ACS APPLIED MATERIALS & INTERFACES

www.acsami.org

Research Article

Enhanced Photothermal Effect Assisted by Resonance Energy Transfer in Carbon/Covellite Core−Shell Nanoparticles toward a High-Performance Interfacial Water Evaporation Process

Suman Chhetri, Anh Tuan Nguyen, Sehwan Song, Dong Hyuk Park, Tianwei Ma, Nicolas Gaillard, Sang-Hee Yoon, and Woochul Lee*

Cite This: *ACS Appl. Mater. Interfaces* 2023, 15, 54773−54785

Read Online

ACCESS | Metrics & More | Article Recommendations | Supporting Information

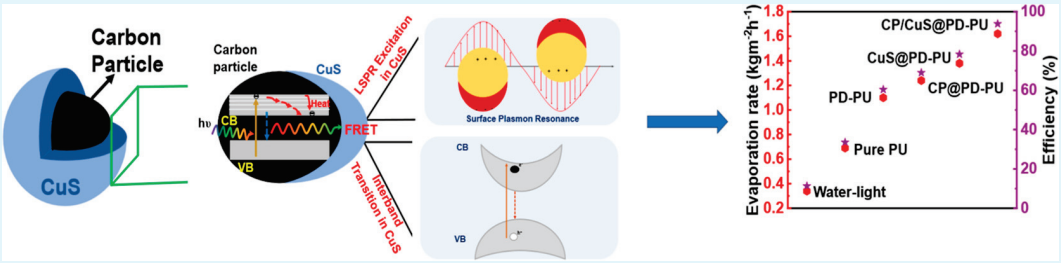

ABSTRACT: Carbon and semiconductor nanoparticles are promising photothermal materials for various solar-driven applications. Inevitable recombination of photoinduced charge carriers in a single constituent, however, hinders the realization of a greater photothermal effect. Core−shell heterostructures utilizing the donor−acceptor pair concept with high-quality interfaces can inhibit energy loss from the radiation relaxation of excited species, thereby enhancing the photothermal effect. Here, core−shell structures composed of a covellite (CuS) shell (acceptor) and spherical carbon nanoparticle (CP) core (donor) (abbreviated as CP/CuS) are proposed to augment the photothermal conversion efficiency via the Förster resonance energy transfer (FRET) mechanism. The close proximity and spectral overlap of the donor and acceptor trigger the FRET mechanism, where the electronic excitation relaxation energy of the CP reinforces the plasmonic resonance and near-infrared absorption in CuS, resulting in boosting the overall photothermal conversion efficiency. CP/CuS core−shell coated on polyurethane (PU) foam exhibits a total solar absorption of 97.1%, leading to an elevation in surface temperature of 61.6 °C in dry conditions under simulated solar illumination at a power density of 1 kW m^{-2} (i.e., 1 sun). Leveraging the enhanced photothermal conversion emanated from the energy transfer effect in the core−shell structure, CP/CuS-coated PU foam achieves an evaporation rate of 1.62 kg m^{-2} h^{-1} and an energy efficiency of 93.8%. Thus, amplifying photothermal energy generation in core−shell structures via resonance energy transfer can be promising in solar energy-driven applications and thus merits further exploration.

KEYWORDS: *core−shell structure, coating, resonance energy transfer, solar absorption, photothermal conversion, solar vapor generation*

INTRODUCTION

Interfacial solar-vapor generation, which uses solar energy to convert water into vapor, is emerging as a sustainable technology for clean water production, particularly in regions where access to freshwater resources is limited.[1−4] The unique feature of this technology lies in the utilization of floating evaporation systems to localize heat at the air−water interface.[5] This localized heat generation in the evaporative region triggers higher solar-to-vapor conversion efficiency compared to conventional evaporation systems, which lose much of their heat to nonevaporative regions such as bulk water.[5] Three key aspects of an interfacial water evaporation system—a solar absorber with broad solar absorption, effective thermal management, and a support structure enabling a continuous water supply—need to synergize to drive maximum solar-vapor conversion efficiency.[6,7] The magnitude of localized heat available for the evaporation process is directly associated with solar light trapping and subsequent photothermal conversion capability of the absorber. In addition, the evaporator design must incorporate a porous, hydrophilic support structure, known as the pumping layer, to convey water to the heating region and an extra insulating layer (typically composed of polymer foams) underneath to restrict heat loss through thermal conduction. Photothermal materials are therefore typically incorporated into porous mediums such as gels,[8] filter

Received: July 23, 2023
Revised: October 9, 2023
Accepted: October 25, 2023
Published: November 15, 2023

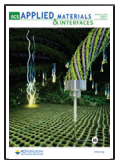

papers,[9] foams,[10] and sponges[11,12] to improve the evaporation rate and vapor generation efficiency. Optimal interfacial evaporators should maximize solar energy harvesting and its conversion to heat through nonradiative relaxation. Carbon materials such as graphite,[13,14] graphene,[15] and CNTs,[16,17] alongside plasmonic nanoparticles,[18−20] semiconductor nanoparticles,[21−24] and conductive polymers[25,26] are frequently used as photothermal materials. However, they tend to have low photothermal conversion efficiency due to rapid charge carrier recombination. More appealing photothermal effects have been achieved with composites of carbon material and inorganic/organic semiconductors, rather than single constituents of inorganic semiconductors or carbon materials.[27,28] In a single component, photogenerated electron−hole recombination is inevitable, leading to most photogenerated charges recombining and releasing energy via radiation relaxation, which leaves only a small proportion of the absorbed solar energy being converted into heat. On the other hand, in composites, one constituent can function as a donor and another as an acceptor, which mitigates fluorescence effects either by inhibiting charge carrier recombination or through resonance energy transfer, leading to enhanced photothermal conversion. Therefore, a composite or heterostructure should be perfectly appropriate as a photothermal material to harvest a wide spectrum of solar energy.

In recent years, a variety of donor−acceptor systems, such as triazine-CNTs and carbon dots-modified MnO_2 nanowires, have been explored to enhance the photothermal effect in interfacial water evaporation.[27,28] Despite these investigations, the development of composites with high-quality interfaces remains a challenge. Inadequate interfacial contact between components can impede charge flow or energy transfer.[29,30] The core−shell heterostructure is considered beneficial for promoting energy transfer and charge separation.[31] The synergistic effect resulting from the strong interfacial electronic interactions in the core−shell structure can leverage efficient charge transfer.[32] Importantly, the close proximity between core and shell constituents renders active interfaces for energy transfer, a requirement for resonance energy transfer. To date, various core−shell structured photothermal materials have been extensively investigated for several applications such as phase-change materials,[33] antibacterial agents, and tumor therapies.[34] A few recent studies on interfacial evaporators, based on magnetic phase-change microcapsules, where the phase-change material as a core is enveloped by a solar absorber-coated magnetic composite shell, have further underscored the potential of core−shell heterostructures in enhancing photothermal effects.[35−38] Nevertheless, the exploitation of the improved photothermal effect originating from the core−shell structure to facilitate the interfacial water evaporation process has yet to be fully examined. In addition, the mechanism driving the elevated heat generation in the core−shell structure has seldom been studied. Considering the potential of core−shell structured photothermal materials in enhancing heat generation via the Förster resonance energy transfer (FRET) mechanism, it is of great interest to tune the solar light absorption capabilities to enable full solar spectrum photothermal conversion.

FRET is a resonant transfer process of electronic excitation energy from a donor component in the excited state to an acceptor in the ground state.[39] The efficiency of FRET is strongly dependent on two factors: the proximity between the donor and acceptor and the extent of overlap between the emission spectra of the donor and the absorption spectra of the acceptor. Herein we report the creation of a core−shell structured photothermal material consisting of covellite (CuS) shells coated over spherical carbon nanoparticle (CP) cores (denoted as CP/CuS), with the aim of enhancing photothermal heat generation via the FRET effect. This study seeks to comprehend how a core−shell structure promotes nonradiative energy transfer and determine whether the process yields a sufficient photothermal effect to enhance the interfacial water evaporation process. The novelty of the present work lies in presenting a proof-of-concept that explores the core−shell structure for a high-performance interfacial evaporator, leveraging enhanced photothermal conversion arising from the resonance energy transfer mechanism. To the best of our knowledge, this is the first report attempting to facilitate the interfacial water evaporation process by leveraging the enhanced photothermal conversion originating from the resonance energy transfer effect in a core−shell structure. The effective spectral overlap between the CP's emission and CuS's absorption spectra supports the energy transfer mechanism in the core−shell structure. An evaporator was designed by coating CP/CuS onto the surface of commercial microporous polyurethane (PU) foam. Owing to the mesoporous network structure of PU and the synergistic photothermal enhancement emerging from the core−shell structure, CP/CuS-coated foam shows a total solar absorption value of 97.1% and an excellent solar-thermal conversion efficiency. The enhanced heat generation on the upper surface of CP/CuS-coated PU foam enables a high vapor generation efficiency of 93.8% and an evaporation rate of 1.62 kg m^{-2} h^{-1} under 1 sun irradiation. Photothermal heat generation via the resonance energy transfer mechanism provides an efficient route to enhance solar energy conversion efficiency and can be employed for applications such as water desalination, purification, sterilization, and power generation.

MATERIALS AND METHODS

Materials. Sodium thiosulfate pentahydrate, cupric sulfate anhydrous, L-ascorbic acid, and dextrose anhydrous were received from Fisher Scientific. Dopamine-HCl and tris(hydroxymethyl) aminomethane (Tris) were purchased from Sigma-Aldrich (USA). PU foam was purchased from United States Plastic Corp. [Item Number: 88642; Porosity: 100 PPI (Pores Per Inch)]. All chemicals used in this work were of reagent grade and used as received without any further purification.

Preparation of CP/CuS. CP/CuS was prepared following a single-step hydrothermal technique, employing a stainless-steel autoclave reactor at 180 °C for 14 h. Briefly, a solution containing 400 mg of $CuSO_4$ and 795 mg of sodium thiosulfate in 60 mL of deionized (DI) water was prepared (solution A). In another beaker, solution B was prepared by dissolving 1140 mg of dextrose and 140 mg of ascorbic acid in 40 mL of water. Solution B was slowly added to solution A under constant stirring. The resulting mixture was transferred into an autoclave and sealed. The autoclave was placed inside a preheated oven (180 °C) for the completion of the reaction and allowed to cool naturally. The as-prepared CP/CuS heterostructure was vacuum-filtered using Whatman filter paper and then dried overnight in an oven at 60 °C. In addition to the CP/CuS heterostructure, single-component materials were prepared using the same procedure. Specifically, pure CuS was prepared using $CuSO_4$ as the copper source and sodium thiosulfate as the sulfur source. Pure CP was prepared using dextrose and ascorbic acid. The CP solution was centrifuged at 10,000 rpm for 10 min, and the solid residue separated from the supernatant was then dried at 60 °C for 12 h to obtain brown-colored CP.

https://doi.org/10.1021/acsami.3c10778
ACS Appl. Mater. Interfaces 2023, 15, 54773−54785

Polydopamine Coating on PU Foam. Polydopamine (PDA) coating on PU foam (PD-PU) was carried out by using a simple dip-coating technique. First, PU foam was cut into a circular shape with a diameter of 5 cm and a thickness of 0.9 cm. The PU foam was immersed in DI water and sonicated for 30 min to get rid of dirt particles, followed by drying in an oven at 60 °C for 12 h. A dopamine solution was prepared by dissolving dopamine hydrochloride (2.0 g/L) in 10 mM Tris buffer solution and its pH was adjusted to 8.5 following a previous report.[40,41] The thoroughly cleaned PU foam was then immersed in the dopamine solution and left for 36 h under constant stirring. This allowed for the autoxidative polymerization reaction of dopamine, resulting in the formation of PDA on the surface of the foam. Next, the coated PU foam was washed with DI to remove free dopamine and loosely held PDA and dried in an oven overnight at 60 °C.

Surface Coating of the Photothermal Layer on PD-PU. CP/CuS coating on PD-PU foam (hereafter, CP/CuS-coated PD-PU is abbreviated as CP/CuS@PD-PU) was performed by a modified drop-casting method. The coating solution was prepared by dispersing CP/CuS in ethanol at a concentration of 10 mg/mL through sonication for about 15 min. The water-soaked PD-PU foam was placed in a preheated oven at 60 °C and then coated with CP/CuS solution using a dropper. The purpose of soaking the PU foam prior to coating was to establish a surface tension gradient between water and ethanol. This gradient restricts the downward diffusion of the solution, ensuring that the coating remains on the upper part of the PU foam.[42] The coating solution was intermittently stirred during drop-casting to prevent the escape of aggregates from the dropper tip, which could lead to the formation of large clumps on the foam surface. To achieve a uniform layer on the upper surface of the foam, we repeated the coating process twice. After drying, a stable coating was achieved on the PD-PU foam due to strong chemical interactions. For comparison purposes, CuS and CP were separately coated on PD-PU foam following the same procedure, which are abbreviated as CuS@PD-PU and CP@PD-PU, respectively.

Characterization Methods. The morphologies of CuS, CP, CP/CuS, and coated foams were observed by a field emission scanning electron microscope (FE-SEM, Hitachi S-4800). The coated foams were mounted on aluminum substrates by using conductive carbon tape and sputter coated with gold/palladium in a Hummer 6.2 sputter coater. SEM was performed at an accelerating voltage of 2.0 kV. The transmission electron microscopy (TEM) image was captured using a Hitachi HT7700 TEM at 100 kV and an AMT XR-41B 2k × 2k CCD camera. The chemical composition of the coated foam was analyzed with an angle-resolved X-ray photoelectron spectroscopy (XPS) system (Theta Probe ARXPS, Thermo Fisher Scientific) equipped with a monochromatic Al Kα source. The analysis was conducted at 200 eV with an analysis spot area diameter of 400 μm. During measurements, the base pressure of the XPS instrument was maintained below 1×10^{-9} mbar. Identification of chemical groups present in PD-PU foams coated with CuS, CP, and CP/CuS was performed by using a Thermo Scientific Nicolet iS10 Fourier transform infrared spectrometer with an attenuated total reflectance accessory (ATR-FT-IR). X-ray diffraction (XRD) spectra were collected by using a Bruker D8 ADVANCE diffractometer with a CuKα source (λ = 1.54060) operating at 40 mA and 40 kV in a parafocusing Bragg–Brentano mode. The measurement was performed with a step size of 0.02° and 4 s per step. The photoluminescence (PL) spectra were acquired by using a custom-made laser confocal microscope (LCM) instrument equipped with SR-303I-B (Andor) and GF-033C-IRF (Allied vision) at λ_{ex} of 405 nm. The samples were placed on a glass substrate, which was mounted on the XY-stage of the systems with a spot size of approximately 200 nm. The scattered light was collected with the same objective lens, and the excitation laser light was filtered out with a long-pass edge filter (Semrock, Rochester, NY, USA). For the quantitative comparison, the incident laser power and the acquisition time for each LCM PL spectrum were fixed at 5 μW and 1 s, respectively, in all measurements. The apparent contact angle of water was characterized by placing a DI water droplet of 2 μL on the uppermost surface of pure and coated PU foam samples. Each sample was purged with N_2 for 10 s before each experiment to remove contaminants. The water contact angle was measured by using the sessile-drop method with a customized goniometer (DSA25S, Krüss GmbH, Germany). Time-dependent water contact angles were acquired by analyzing the sequential images with an image processing program, ImageJ (National Institutes of Health, USA), together with its Drop Snake plugin. All measurements were conducted in a chamber with a controlled temperature (22 ± 1 °C) and relative humidity (50 ± 5%). For each sample, the water contact angle was measured at least 10 times and the average value was reported. The transmittance (T) and reflectance (R) of the coated PU foam samples were measured by using a UV–vis–near-infrared (UV–vis–NIR) spectrophotometer with an integrating sphere in the wavelength range of 280–2500 nm (PerkinElmer LAMBDA 750 S UV/vis/NIR spectrophotometer). The absorption (A) of the samples was calculated from the relationship $A = 1 - R - T$. Furthermore, total solar absorption a_{tot} was calculated with reference to the spectral solar irradiance density of air mass 1.5 global (AM 1.5 G) tilt solar spectrum, using the following expression

$$a_{tot} = \frac{\int_{280}^{2500} I_\lambda A_\lambda \mathrm{d}\lambda}{\int_{280}^{2500} I_\lambda \mathrm{d}\lambda}$$

where I (W m^{-2} nm^{-1}) is the solar spectral irradiance, λ (nm) is the wavelength, and A_λ is the absorption efficiency at a given wavelength of λ.

Evaluation of Evaporation Performance of Pure and Coated Foams. The photothermal evaporation performance of the coated PU foams was tested under an ambient condition of 24 °C temperature and 50% relative humidity. A solar simulator (Oriel Instruments) equipped with a Xe bulb and an AM1.5G filter (91192-1000, Newport) was used as the illuminator. A NREL-calibrated Si photodiode was used to calibrate the intensity of solar irradiation (1 sun illumination, 1 kW m^{-2}) on the sample. An evaporation system, which consists of a water container (beaker), a 6 mm thick polystyrene foam support as a thermal insulator, coated PU foam with the photothermal layer, and a cotton wick serving as a path for water transport, was placed under the solar simulator. A circular hole with a diameter of 1.5 cm was made at the center of the polystyrene foam to support the cotton wick. The coated PU foam was placed on the polystyrene foam support, ensuring that the upper surface was exactly on the brim of the beaker. The evaporation system was positioned on a software-controlled electronic balance (AGCN220, accuracy 0.1 mg, TORBAL, USA) to record the mass change of water. In addition, a thermocouple (OM-HL-EH-TC, OMEGA) was used to measure the temperature of bulk water before the experiment and during the evaporation process. To establish a steady-state water absorption rate, the coated foams were prewetted with water by using a dropper before the experiment. A high-resolution infrared camera (SC655, FLIR) was employed to monitor the surface temperature of the evaporator during illumination. The camera was operated in video mode to record spatial and temporal temperature changes on the surface of the evaporator during evaporation. The evaporation rate per unit area, $\dot{m}$, was calculated using the following equation[24]

$$\dot{m} = \frac{4m_{loss}}{\pi D^2 t}$$

where m_{loss} represents the weight losses of the water due to evaporation, D is the diameter of the evaporator (identical to the aperture size), and t represents the irradiation time for each water evaporation experiment.

RESULTS AND DISCUSSION

Structural and Morphological Characterization of CuS, CP, and CP/CuS. The structural and morphological characterization of CuS, CP, and CP/CuS was performed by using various techniques. The presence of functional groups

https://doi.org/10.1021/acsami.3c10778
ACS Appl. Mater. Interfaces 2023, 15, 54773–54785

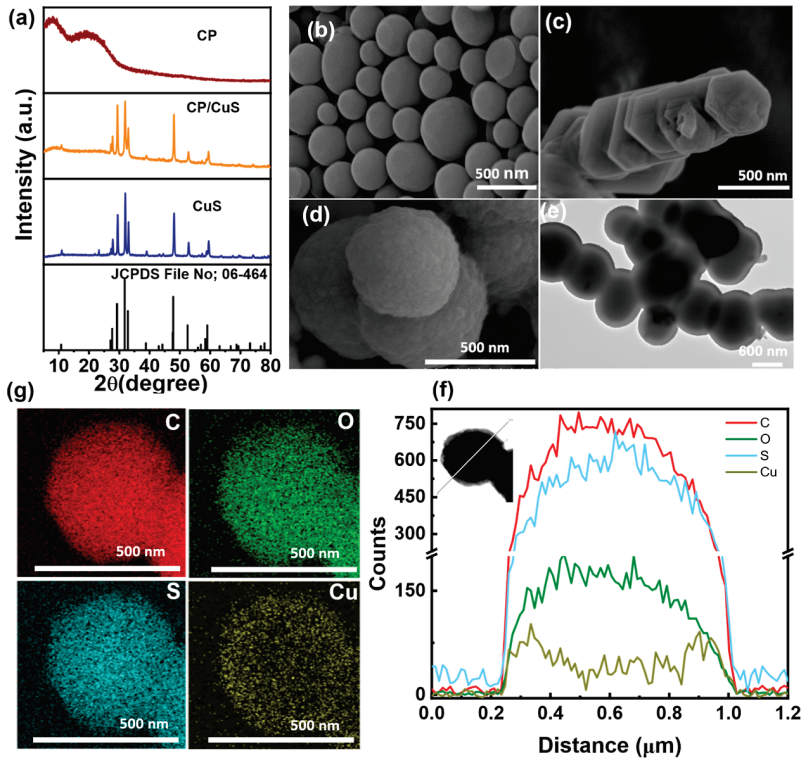

Figure 1. Structural and morphological studies of prepared photothermal materials. (a) XRD pattern of CuS, CP, and CP/CuS heterostructure. The major diffraction peaks of CuS and CP/CuS are indexed to crystal planes of covellite CuS (JCPDS 060464), which reveal the crystalline phase of CuS in the heterostructure. (b–d) SEM images of (b) CP, (c) CuS, and (d) CP/CuS, (e) TEM micrograph of the CP/CuS heterostructure, and (f) EDS line-scan profiles of the CP/CuS core–shell structure marked in the inset figure, where the light gray line represents the position of the line-scan. (g) EDS elemental mapping of the CP/CuS core–shell structure. The elements present are labeled on each image. Red, green, blue, and gold colors represent carbon, oxygen, sulfur, and copper components, respectively.

and chemical linkages/interactions in the materials was investigated by using Fourier transform infrared spectroscopy (FT-IR). Figure S1 shows the FT-IR spectra of CuS, CP, and CP/CuS. The stretching bands present at 3133, 3009, 2947, 1729, 1455, and 1111 cm^{-1} indicate the presence of −OH, −CH (sp^2), −CH (sp^3), −C═O, −C═C, and −C−O groups in CP. These same stretching bands were also found in CP/CuS, along with an additional small peak at 606 cm^{-1}, indicating the presence of Cu−S stretching modes.[43,44] The crystal phase of CuS, prepared by using the hydrothermal method without surfactants, was confirmed by powder XRD patterns, as shown in Figure 1a. The diffraction peaks at 2θ values of 27.7, 29.3, 31.8, 32.9, 38.8, 47.9, 52.7, and 59.3° are ascribed to the (101), (102), (103), (006), (105), (110), (108), and (116) crystal planes of the hexagonal covellite CuS crystal phase (JACPDS card no. 06-464). No specific peaks related to other copper sulfide phases are observed, indicating the formation of pure hexagonal phase covellite. The sharp diffraction peaks indicate the highly crystalline nature of the prepared CuS. The XRD pattern of CP/CuS showed the same peak pattern as that of CuS, with an additional hump at an angle of 8.1° due to the graphitic plane (001) of CP. The broad XRD peak of CP centered at approximately 21° corresponds to (002) reflection, indicating the turbostratically disordered structure of spherical CP.[45] The broad (002) peak incorporates diffuse sets of interlayer distances that are greater than those in crystalline graphite.[46]

The microstructure and morphology of CuS, CP, and CP/CuS were investigated by SEM and TEM analyses. SEM images in Figure 1b show the highly uniform spherical shapes of the as-obtained CP, with diameters ranging from 167 to 507 nm. CuS nanostructures exhibit a well-arranged petal-like 3-dimensional flower morphology (Figure S2a). Careful examination of this structure reveals that it is composed of hexagonal CuS nanoplates with various lengths and an average thickness of approximately 191 nm, as seen in the SEM image (Figure 1c). The SEM image in Figure 1d shows the CP/CuS core–shell heterostructure. The deposition of CuS nanoparticles on the smooth CP led to the roughening of the surface and an increase in the diameter. It appears that during the formation of CP/CuS, some CuS nanoplates did not adhere to the CP surface, resulting in their random arrangement and aggregation (Figure S2b). To further examine microstructural features and confirm the core–shell structure, CP/CuS was inspected by TEM. The TEM images of CP/CuS show a distinct biphasic material with a dense core enveloped by a uniform shell (Figure 1e). Additionally, numerous CuS particles were found to aggregate around the CP/CuS heterostructure (Figure S2c), which agrees well with the morphological features observed in the SEM analysis. It is worth noting that no interlayer gap between CuS and CP is observed, signifying the firm adherence of CuS to the CP structure and the formation of a high-quality interface. This core–shell structure of CP/CuS was further supported by TEM energy-dispersive spectroscopy (EDS). Figure 1f shows EDS line scanning spectra of CP/CuS, obtained along the line represented in the inset. The C spectrum shows a symmetric shape, with the peak centered at the core of the

https://doi.org/10.1021/acsami.3c10778
ACS Appl. Mater. Interfaces 2023, 15, 54773−54785

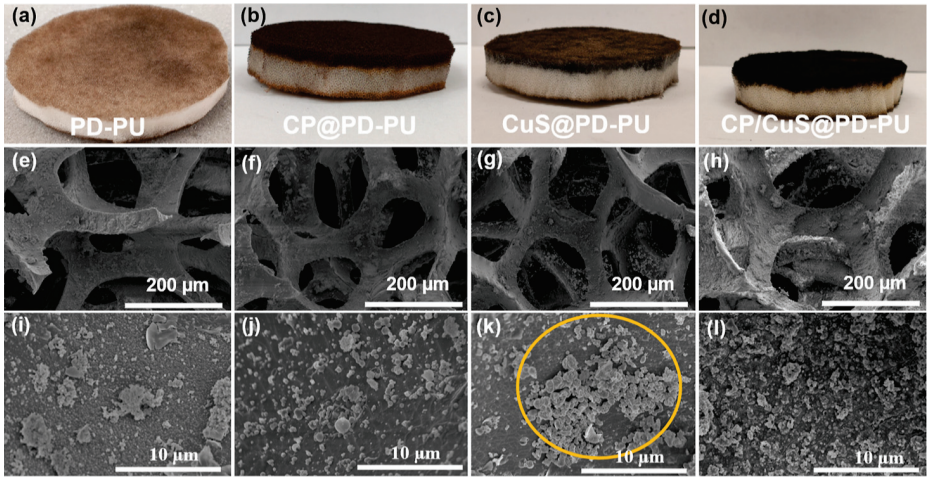

Figure 2. Fabrication of the photothermal layer-coated evaporators and their morphological characterization. Digital images of (a) PDA-coated PU (PD-PU), (b) CP-coated PD-PU, (c) CuS-coated PD-PU, and (d) CP/CuS-coated PD-PU. Image (a) depicts the surface and tilted view of the PDA-coated PU, wherein a thin layer of coating is present only on the top and bottom surfaces of the foam. Images (b–d) show the surface localized coating of CP, CuS, and CP/CuS heterostructure on PD-PU. (e–h) SEM micrographs of (e) PDA-coated PU, (f) CP coating on PD-PU, (g) CuS coating on PD-PU, and (h) CP/CuS heterostructure coating on PD-PU. (i–l) Enlarged SEM image of (i) PDA-coated PU, (j) CP-coated PD-PU, (k) CuS-coated PD-PU, and (l) CP/CuS heterostructure-coated PD-PU. (i) Self-polymerization of dopamine on PU foam forms spherical-shaped particles of PDA. (j) The CP uniformly covers the PD-PU foam surface, but interfacial adhesion does not appear robust. (k) The yellow circle demonstrates the aggregates of CuS nanoparticles on the PD-PU foam surface. (l) The firmly entrenched CP/CuS particles on the PD-PU surface indicate the strong interfacial interaction between the CP/CuS heterostructure and PD-PU foam.

heterostructure. On the other hand, the Cu spectrum exhibits saddle-shaped symmetry with two side peaks indicating higher intensity in the outer region (i.e., shell). The considerable amount of carbon signal in CP/CuS is attributed to the core of the structure consisting of CP. Nanoscale elemental mappings also support the core–shell structure, as shown in Figure 1g, where Cu is confined to the outer region while carbon is in the inner region. It is expected that the synergistic interactions between core (CP) and shell (CuS) components would promote resonance transfer mechanisms, suppressing radiative recombination and increasing the photothermal conversion, which we will demonstrate later.

Characterization of the Photothermal Layer Coating. Evaporators were prepared by sequentially depositing different photothermal layers on PU foams, which served as the pumping layer. In short, a thin layer of PDA was solution coated on both sides of PU foam, followed by a secondary coating of the photothermal material (i.e., CP/CuS, CP, and CuS) on the top side of the foam. PDA coating on the lower part of PU foam increases its hydrophilicity, facilitating water pumping to the PU foam and quick replenishment of evaporated water. Though photothermal materials loaded onto foam or sponge supports have shown considerable water evaporation efficiency,[47] a drawback of this approach is the potential for the loadings to detach from the support under prolonged irradiation due to the poor physical or chemical interaction between the upper photothermal layer and the lower porous pumping layer. To address this issue, the surface of the support can be chemically activated to enhance its stability with the loaded photothermal layer. In this context, the catechol, amine, and imine groups in PDA are expected to secure the loaded core–shell CP/CuS to the PU foam support through hydrogen bonding interactions and complexation.[40,48] In addition to serving as a template for stable secondary coating, the PDA layer also enhances the light-absorption ability of the coated foams, contributing to the achievement of broadband absorption.[49] The core–shell heterostructure, created by enclosing CuS around the CP, proved to be effective in inhibiting the agglomeration. This facilitated a homogeneous dispersion of CP/CuS in ethanol (Figure S3a), which promoted a uniform coating on the PU foam surface. The CP/CuS dispersion in ethanol formed a stable solution, and no particle sedimentation was observed after 12 h (Figure S3b). In contrast, CuS in ethanol began to settle down after 1 h (Figure S3b), necessitating continuous agitation while coating to ensure uniform spreading of CuS on the PD-PU surface.

The sequential deposition of the photothermal layer changed the color of the PU foam. It transitioned from white to dark brown after the initial PDA coating. A digital image of the as-prepared PU foam is displayed in Figure S4a. Figure 2a shows the uniform PDA layer on the foam surface, including the cross-sectional view of the space between the upper and lower surfaces of PD-PU. Digital images shown in Figure 2b–d depict the coatings of CP, CuS, and CP/CuS on the upper side of PD-PU. It is clearly discernible from the images that the coating is solely confined to the top surface of the foam, while the bottom surface consists only of a layer of PDA. SEM images of the coated PU foam at varying magnifications are shown in Figure 2e–l. The SEM micrograph of the prepared PU foam exhibits a highly porous network structure with a smooth skeleton (Figure S4b). On the other hand, the surface of the PDA, CP, CuS, and CP/CuS-coated foams appears rough, indicating the successful anchoring of particles onto the foam skeletons (Figure 2e–h), a trait favorable for light absorption and water transportation. The self-polymerization of dopamine forms a coating of spherical PDA particles on the PU foam, as shown in the magnified image (Figure 2i). The dense and uniform coating of PDA provides a template for further interactions, which is expected to facilitate the adhesion of CP (Figure 2f), CuS (Figure 2g), and CP/CuS (Figure 2h) to the PU foam. The uniformly

https://doi.org/10.1021/acsami.3c10778
ACS Appl. Mater. Interfaces 2023, 15, 54773–54785

deposited spherical CP on the PDA-coated PU surface suggest the firm adherence provided by the PDA template to CP (Figure 2j). On the other hand, the enlarged microstructure of CuS-coated PD-PU skeletons shows agglomerate and sparsely populated regions of nanoparticles, as indicated by a circle in Figure 2k. This could be due to its inhomogeneous dispersion in the coating solution. Despite the less stable CuS dispersion in ethanol compared to CP and CP/CuS, the CuS on PD-PU foam allowed a firm and durable coating, likely due to the immobilization of CuS on the PDA template via complexation.[50] The deposition of CP and CP/CuS on PD-PU appears to be more uniform and seamless in the foam skeleton. The enlarged SEM image (Figure 2l) further confirms the uniform CP/CuS coating on PU foam without evident aggregation and the firm anchoring of CP/CuS particles on the PDA template. Uniform deposition of the photothermal material on the porous structure is beneficial for interfacial water evaporation, as the evenly coated particles keep the capillary channels open. It is worth noting that the PU foam maintains its initial interconnected porous structure, even after the coating process. There were no signs of foam skeleton swelling or pore shrinkage resulting from the coating process. Hence, the coating process only altered the surface properties, such as wettability and roughness of the foam, without affecting its initial 3D framework. The well-maintained porous structure combined with the rough skeleton is expected to promote light absorption and play a crucial role in water replenishment for evaporation.

FT-IR and XPS were employed to determine the chemical compositions of the coatings on the PU foam. As shown in Figure 3a, the FT-IR curves for both as-prepared and coated

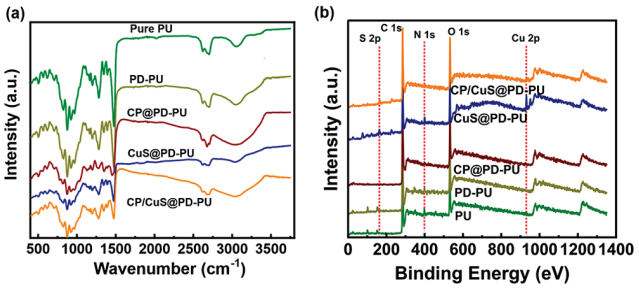

Figure 3. Characterization of coated PU foams. (a) FT-IR and (b) XPS measurements of pure PU, PDA-coated PU, CP-coated PD-PU, CuS-coated PD-PU, and CP/CuS heterostructure-coated PD-PU.

PU foams show a broad peak centered at 3311 cm^{-1} and a small peak at 1729 cm^{-1}, which are ascribed to the stretching band of N−H and −C═O stretching of the urethane, respectively. Interestingly, the N−H stretching peak disappeared upon PDA coating, possibly due to the hydrogen bond interaction between the polar functionalities of PDA and PU foam. The elemental composition of PU foam before and after surface coating was further investigated by XPS and the corresponding spectra are presented in Figure 3b. Three characteristic peaks observed at 284, 398.9, and 531 eV correspond to binding energies of C 1S, N 1S, and O 1S, which are the main constituent elements of PU foam.[12,51] The deconvoluted peaks are presented in Figure S5a−c. After PDA coating on the PU foam, a notable increase in the intensity of the N 1s was observed, as reflected in the area under the deconvoluted N 1s peak: 66.1% in PD-PU against 31.7% in as-prepared PU (Figures S5c and S6c). This evidence confirms the successful deposition of PDA on the PU surface. The deconvoluted C 1s peak in PD-PU shows peaks at 284.01, 285.6, 287.2, and 288.6 eV, which are attributed to sp^2 graphitic carbon in PDA, carbon in C−O, C═O, and in the conjugated system, respectively (Figure S6a). The O 1s spectrum is deconvoluted into peaks 532.5 and 531.3 eV, corresponding to catechol groups (C−OH) and quinone groups (C═O), respectively (Figure S6b).[52,53] As for N 1s, the peak at 399.1 eV is ascribed to the N−H groups in PDA. The spectra of CuS@PD-PU and CP/CuS@PD-PU show peaks at 933 and 164 eV, corresponding to Cu 2p and S 2p, respectively (Figure 3b). The high-resolution peaks of the elements present in CuS-, CP-, and CP/CuS-coated PD-PU are presented in Figures S7−S9. The high-resolution Cu 2p spectrum (Figure S9e) shows two peaks at 933.2 and 952.8 eV, which are assigned to Cu $2p_{3/2}$ and Cu $2p_{1/2}$, respectively.[54] For the S 2p spectrum, the deconvoluted peaks at 163.2 and 164.5 eV are typical values for metal sulfides (Figure S9d).[54]

Maintaining a continuous water supply to the evaporative region (i.e., the upper surface) is crucial for a high-performance evaporator, and this supply is largely influenced by surface wettability. As depicted in Figure 4a,b, the contact angles for PU and PD-PU are 118.5° ± 8.2 and 105.2° ± 9.2, respectively. Enhanced hydrophilicity of PD-PU, compared to PU, could be attributed to the presence of abundant functional groups such as catechol, amine, and imine in PDA. Furthermore, the contact angle of PD-PU foam drops to less than 90° within 15 s, indicating its favorable wettability. Coating CuS and CP on PD-PU results in contact angles of 121.8° ± 12.4 and 124.8° ± 8.4, respectively (Figure 4c,d), indicating more hydrophobic surfaces. Carbon content makes the surface of CP@PD-PU more hydrophobic. For CuS@PD-PU, a higher contact angle may be due to the agglomeration of CuS nanoparticles in some regions of the foam. Interestingly, CP/CuS heterostructure-coated PD-PU exhibits a lower contact angle of 79.8° ± 10.7° (Figure 4e). Moreover, the contact angle decreases rapidly to 17.5° within 1 s, with the water droplet infiltrating the foam and disappearing within 1.25 s (Figure 4m_1−m_3). Video S1 captures the dynamics of water spreading and its movement on the CP/CuS@PD-PU foam. The desirable wettability of the CP/CuS@PD-PU foam, offered by the synergistic merits of the core−shell heterostructure, is beneficial for the horizontal spread of water and hence for replenishment during the evaporation process. A balance between hydrophilic and hydrophobic properties is imperative to ensure an uninterrupted water supply. If the upper surface is too hydrophobic, it could inhibit the water replenishment process, while a highly hydrophilic surface could increase the work for evaporation, thereby retarding the escape of vapor.

Solar Light Absorption and Photothermal Studies of Coated Foams. The efficient absorption of solar light over a broad wavelength range and its conversion to thermal energy are of paramount importance for a photothermal material to drive localized water evaporation. Therefore, the light absorption ability of the pure and coated PU foams was evaluated via UV−vis−NIR spectrophotometry in the wavelength ranging from 280 to 2500 nm. Then, the total solar absorptions of all the studied samples were calculated. As displayed in Figure 5a, PU foam shows very weak solar absorption, whereas coating a layer of PDA (PD-PU) leads to a significant enhancement in the absorption (~88.2%),

https://doi.org/10.1021/acsami.3c10778
ACS Appl. Mater. Interfaces 2023, 15, 54773−54785

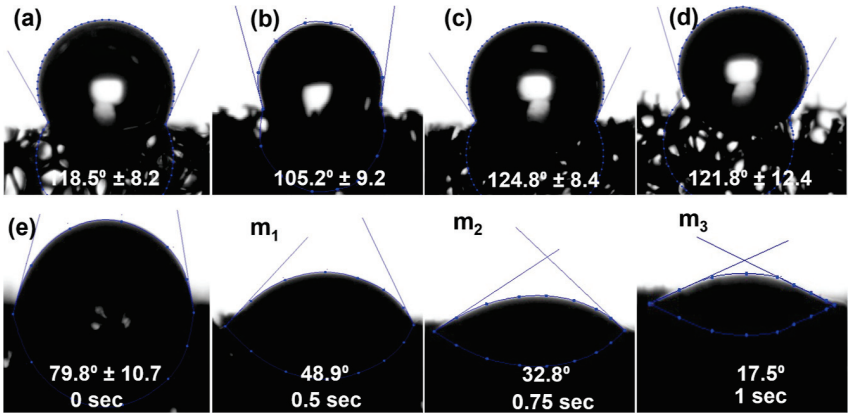

Figure 4. Photographs of water droplets on pure and coated foam and their contact angle measurement. Surface wettability of (a) pure PU, (b) PD-PU, (c) CP@PD-PU, (d) CuS@PD-PU, and (e) CP/CuS@PD-PU coated foam surface. The heterostructure CP/CuS-coated PU foam showed remarkable water affinity with a contact angle value of 79.8°. The contact angle value represented here is the average calculated from at least five measurements made in different regions of the foam surface. Both right and left angle measurements were taken into consideration when calculating the average value. Images (m_1−m_3) depict the time-dependent water contact angle on the CP/CuS heterostructure-coated PD-PU. The water contact angle decreased to 17.5° within 1 s and the water droplet disappeared in 1.25 s.

especially in the UV−vis and near-IR region, which is characteristic of PDA.[55] It is worth noting that additional coating of CP on PD-PU results in a slight increase in visible region absorption and a small decrease in near-IR region absorption, aligning well with previous findings.[55] The deposition of CuS on PD-PU (CuS@PD-PU) yields a significant increase in absorption to 98 and 93% in the UV−vis and IR regions, respectively, resulting in a total solar absorption of ∼96%. This improved absorption in the entire studied spectral range can be attributed to the localized surface plasma resonance (LSPR) absorption in the visible region and the interband transitions characteristic of covellite in the near-IR region.[56−58] The CuS-coated PD-PU's absorption surpasses that of CuS plasmonic membranes (89.3%),[24] CuS/PE membranes (93%),[59] and cotton-CuS nanocages (94−95.5%).[60] It has been reported that LSPR is not only limited to plasmonic metals (such as Cu and Au) but also occurs in semiconductors, such as chalcogenides and metal oxides.[58,61] In principle, semiconductor nanostructures are expected to display LSPR properties similar to those of metals.[61] Therefore, in the case of CuS-coated PD-PU, both plasmonic hole oscillation and interband electronic transitions of CuS contribute to enhanced light absorption.[62]

In the presence of the CP/CuS core−shell structure, the absorption efficiency of CP/CuS@PD-PU foam increases up to 98.9% in the UV−vis region and greater than 94% in the IR region, which is higher than the absorption of either CuS@PD-PU or CP@PD-PU. The improved solar light absorption can be attributed to individual absorption characteristics of CP in the UV−vis region and CuS in the IR region, as well as the synergistic effect from the core−shell structure. Absorption characteristics of CP/CuS@PD-PU suggest that the presence of CP may enhance both LSPR and interband transitions in CuS, synergistically boosting the overall absorption of CuS. Apart from the coated photothermal material, the porous structure of PU foam also aids in trapping light through multiple scattering within its micropores. Furthermore, the higher absorption can be justified by the low reflectance of the CP/CuS-coated foam (Figure S10a) (1.1% in UV−vis and 5.5% in IR region) and negligible transmittance of less than 0.1% (Figure S10b), which result from the formation of the rougher heterostructure coating. The excellent absorption efficiency indicates that the formation of a core−shell heterostructure results in novel synergistic effects, which could facilitate heat accumulation for water evaporation, making our proposed material promising for interfacial solar-vapor evaporators.

The nonradiative relaxation of absorbed light leads to local heating of the lattice, resulting in temperature elevation, which serves as a measure of the photo-to-heat conversion efficiency of the photothermal material. To quantify the photothermal performance of coated PU foams, time-dependent surface temperature distribution under 1 sun radiation was measured using an IR camera in dry conditions (i.e., foams are dry). Figures 5b and S11a−e show the temperature variations and the thermal images obtained after 2 min of simulated solar irradiation. As depicted in Figure 5b, PU foam, which has minimal light absorption and heat conversion, shows a temperature rise to 33.3 °C. In contrast, temperatures of coated PU foams rise quickly and reach near equilibrium after 2 min of illumination at a power density of 1 kW m^{-2} (i.e., 1 sun). The coated foams, PD-PU, CP@PD-PU, CuS@PD-PU, and CP/CuS@PD-PU, exhibit near-equilibrium surface peak temperatures of approximately 64.5, 71.1, 82.5, and 85.6 °C, respectively. A summary of all of the studied properties is provided in Table S1. It is believed that due to the interactions between the surface functional groups, the assembly of CP creates a series of energy sublevels between the conduction band (CB) and valence band (VB).[63] As a result, the CP assemblies promote the nonradiative relaxation of excited charge, leading to the release of heat energy and, in turn, enhancing the photothermal conversion in CP@PD-PU compared to PD-PU. The higher photothermal effect of CuS@PD-PU compared to CP@PD-PU can be attributed to the enhanced light absorption exhibited by CuS, owing to LSPR and band gap absorption. Energetic electrons, generated by LSPR through nonradiative decay and band gap relaxation, collectively contribute to the amplified photothermal effect in CuS@PD-PU. The greater temperature elevation exhibited by CP/CuS@PD-PU, compared to the individual components (namely, CP@PD-PU and CuS@ PD-PU), suggests that the CP/CuS core−shell structure produces more thermal energy.

https://doi.org/10.1021/acsami.3c10778
ACS Appl. Mater. Interfaces 2023, 15, 54773−54785

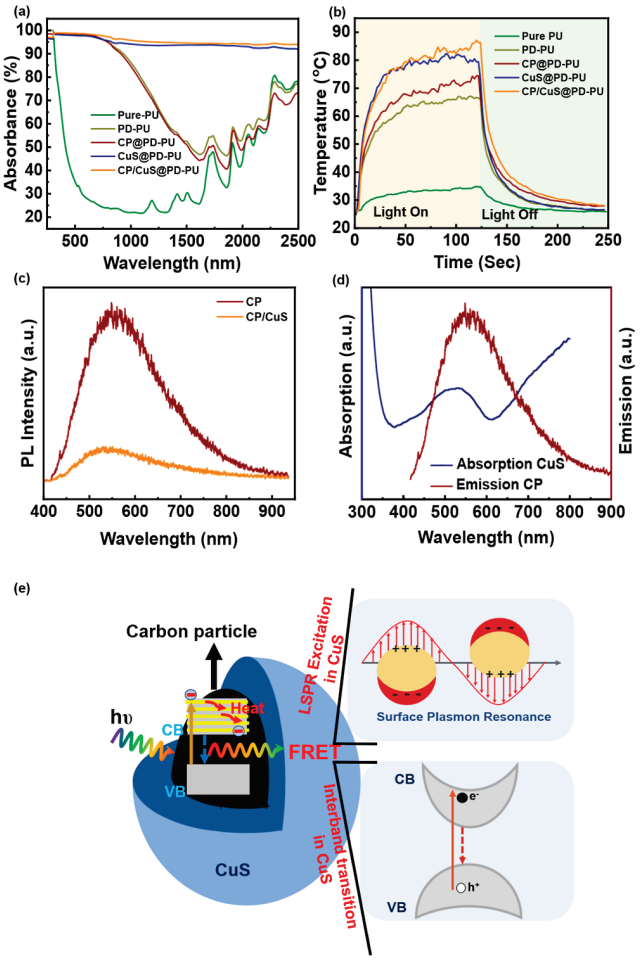

Figure 5. Optical characterization and photothermal studies of prepared evaporators. (a) UV−vis−NIR absorption of pure and coated PU foams in a full wavelength range of 280−2500 nm. (b) Time-dependent surface temperature of pure and coated PU foams. Temperature was recorded for 4 min, where the irradiation was on for the first 2 min and off for the subsequent 2 min. (c) PL spectra of the CP and CP/CuS under 405 nm of excitation wavelength. The diminished PL intensity in the case of the core−shell structure compared to the intensity in the CP indicates the resonance energy transfer effect. (d) Absorption spectra of CuS in ethanol solution and PL emission spectrum of the CP. (e) Schematic showing the resonance energy transfer mechanism in the CP/CuS core−shell structure with the CP as a donor and CuS as an acceptor. The energy released due to the relaxation of excited electrons in the CP gets transferred to CuS through FRET. The transferred energy augments both LSPR excitation and interband transition in CuS, enhancing the overall photothermal conversion.

This could be possible due to the reduction of radiative recombination of photoexcited charges via charge transfer or resonance energy transfer.[55] This indicates that beyond the heat generation due to band relaxation, there is an additional potential reason for the higher surface temperature of CP/CuS@PD-PU. Therefore, it becomes crucial to explore the mechanism that facilitates extra thermal energy in the CP/CuS core−shell structure.

Mechanism for the Enhanced Photothermal Effect. PL measurements were employed to examine the contribution of the special CP/CuS core−shell structure to promoting the enhanced photothermal effect. As presented in Figure 5c, the CP shows strong PL intensity at an excitation wavelength of 405 nm, which is significantly reduced in the CP/CuS core−shell structure. Fluorescence quenching is generally attributed to either an electron transfer mechanism or an energy transfer mechanism, such as FRET.[64] The diminished PL intensity in CP/CuS also indicates a reduced recombination of electron−hole pairs. Given that the realization of a direct electron transfer mechanism necessitates energy level matching, investigation of the energy transfer in a core−shell structure becomes crucial as it can promote electron−hole pair generation and plasmon resonance in semiconductors. The conditions requisite for FRET to occur are the close proximity between the components, and importantly the energy emission spectrum of the donor (CP in this case) must overlap with the absorption or excitation spectrum of the acceptor (CuS, in this instance).[65] The extent to which the donor−acceptor pairs overlap is termed the spectral overlap integral. The excellent overlap between the emission spectrum of CP and the absorption spectrum of CuS, as shown in Figure 5d, supports that FRET is the primary mechanism of energy transfer, thereby enhancing the photothermal conversion in the CP/CuS core−shell structure. Here, the CP donor emits a maximum emission at 555.7 nm, while the CuS acceptor shows a maximum absorption centered around 520 nm. Thus, the energy emitted by the CP core is predominantly absorbed by the CuS shell. It is likely that the energy released due to the relaxation of excited charges in CP resonates with the LSPR of CuS nanoparticles, thereby enhancing absorption and, in turn, the photothermal conversion. As previously reported, the LSPR effect contributes to increased electron or hole vibration, converting irradiated light into thermal energy.[66,67] This significant increase in surface temperature can, therefore, be partially ascribed to the LSPR effect, accelerating the photothermal conversion. In addition, the FRET process may also nonradiatively excite additional electron−hole pairs in CuS, and its subsequent relaxation in lower energy levels boosts photothermal effect. Thus, the resonance energy promotes LSPR and hot-electron generation and increases electron−hole pairs in CuS increasing the overall photothermal effect.

Therefore, reinforced photothermal conversion in the CP/CuS core−shell structure is believed to proceed via FRET. Resonance energy released due to the relaxation of excited charges in the CP is transferred to CuS, enhancing the LSPR effect and initiating electron and phonon oscillation. The resonance energy transfer effect in the core−shell structure provides a novel path for improving photothermal conversion efficiency. Figure 5e illustrates the resonance energy transfer mechanism within the CP/CuS core−shell structure. Upon light absorption by the donor, the CP, an electron from the ground state jumps to a higher vibrational level, then undergoes rapid relaxation to the lower vibrational levels while dissipating the reorganization energy and eventually returns to the ground state. It is known that for the resonance energy transfer mechanism to take place, a resonance condition needs to be satisfied, wherein the oscillation of the excited CP resonates with the ground state electronic energy gap of CuS. The transfer of resonance energy from the CP to CuS leads to electron excitation, followed by vibrational relaxation, and subsequent return to the ground state, emitting photons. It is worthwhile to mention that this mechanism is highly efficient in enhancing solar energy conversion efficiency, as it is not constrained by the need for a suitable electronic band structure match; crucial to achieve enhanced energy transfer is the

https://doi.org/10.1021/acsami.3c10778
ACS Appl. Mater. Interfaces 2023, 15, 54773−54785

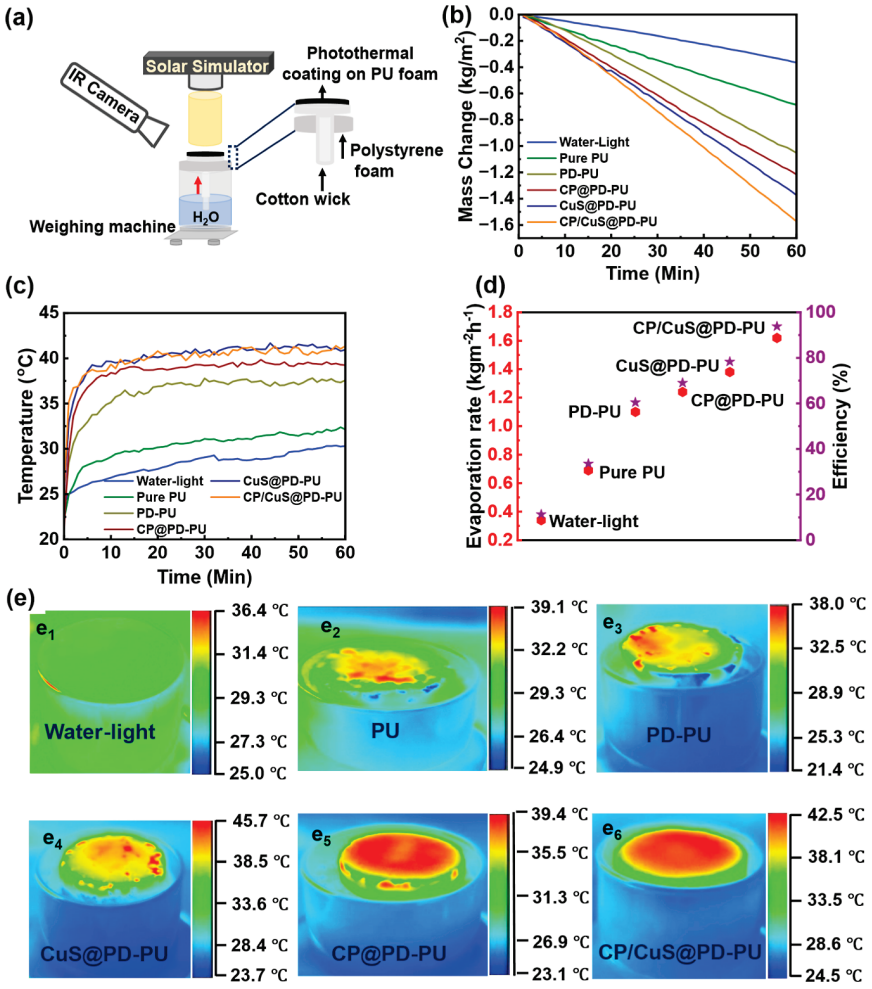

Figure 6. Characterization of the water evaporation performance under 1 sun illumination. (a) Schematic of the experimental setup for the solar-driven water evaporation. (b) Time-dependent mass change for pure PU and coated PU foams. (c) Surface temperature changes of pure water, pure PU, and coated foams over time. (d) Evaporation rates and the corresponding solar-to-vapor conversion efficiencies. (e) Thermal images of (e_1) the pure water, (e_2) pure PU, (e_3) PD-PU, (e_4) CuS@PD-PU, (e_5) CP@PD-PU, and (e_6) CP/CuS@PD-PU after 1 h.

proximity and spectral overlap of the donor and acceptor. In the present case, the emission peak (PL) of CP/CuS demonstrates a blue shift in comparison to the CP, suggesting strong interactions between the CP and CuS. As reported, such interactions can modify the surface states of the interacting components, generating a series of sublevels between conduction and valence bands. This process suppresses the radiative recombination of the photoexcited charges, leading to the release of thermal energy.[42,55] Our experimental results support a hypothesis that a core−shell structure with robust interaction has the potential to achieve optimal photothermal conversion, suitable for a range of solar energy harvesting applications.

Solar-Powered Evaporation Performance. The enhanced photothermal effect emanated from resonance energy transfer in a core−shell structure and the excellent stability of the coated PU foam ushered in the development of an evaporator for interfacial water evaporation. For comparison, interfacial water evaporation performance of PD-PU and CP- and CuS-coated PD-PU was also characterized. A schematic of the solar water evaporation experimental setup is presented in Figure 6a. In order to calculate the evaporation rate precisely, the light spot size was adjusted to match the photothermal surface using an appropriately sized aperture. Water evaporation rates for the coated PU foams were measured by recording the change in water mass over time during solar illumination, and the results were compared with those of pure PU foam and pure water. Figure 6b presents representative plots of time-dependent changes in water mass, and Figure 6d represents the corresponding evaporation rates. The mass change of water in the dark condition is presented in Figure S12 (0.164 kg m^{-2} h^{-1}). CP/CuS@PD-PU demonstrated the highest evaporation rate (1.62 kg m^{-2} h^{-1}) compared to CuS@PD-PU (1.38 kg m^{-2} h^{-1}) and CP@PD-PU (1.24 kg m^{-2} h^{-1}), while PD-PU and pure PU exhibits 1.1 and 0.69 kg m^{-2} h^{-1}, respectively. The evaporation rate of PD-PU is comparable to the rates exhibited by PU sponge-PDA and melamine sponge-PDA.[12,68] In addition, the evaporation rate of CuS@PD-PU is close to the values shown by the CuS-poly(vinylidene fluoride) membrane and hollow CuS-melamine foam.[24,69] Apart from the excellent heat generation by the core−shell heterostructure, the higher evaporation rate of CP/CuS@PD-PU can be attributed to its optimal wettability, responsible for facilitating consistent water supply and accelerating vapor escape. Figure 6c shows the temperature distribution across the surface of the pure and coated PU foams during the evaporation process (1 h of simulated solar light irradiation). Thermal images acquired during the process are presented in Figure 6e (e_1−e_6). The

https://doi.org/10.1021/acsami.3c10778
ACS Appl. Mater. Interfaces 2023, 15, 54773−54785

surface of water alone (without the foam) exhibits a temperature of 28.7 °C, whereas the pure PU foam shows 31.6 °C corresponding to increments of 4.9 and 7.8 °C against the ambient temperature (~24 °C), respectively. Compared to CuS@PD-PU and CP@PD-PU, the surface temperature of CP/CuS@PD-PU increases sharply during the initial transient period but moderates to a level between those of CuS@PD-PU and CP@PD-PU in the steady state. The bulk water temperature, measured by a thermocouple after 1 h, shows an increase of ~3 °C, which can likely be due to energy loss through the cotton wick. Surface peak temperatures recorded for CuS@PD-PU, CP@PD-PU, and CP/CuS@PD-PU are 40.4, 39.8, and 40.3 °C, respectively. The slightly higher surface temperature exhibited by CuS@PD-PU can be attributed to the agglomerated CuS nanoparticles in some regions on the PU foam, likely reducing the water affinity and subsequently inhibiting the water supply to these regions. Once the water evaporates from these areas, the replenishment process takes time, during which these sections remain relatively dry. The higher temperature recorded by these dry surfaces can be verified through the thermal image of CuS (Figure 6e$_4$), showing patches of higher temperature implying temperature variation across the CuS-coated PD-PU foam surface. Similar observations of dry surfaces recording higher surface temperatures due to a suppressed evaporation rate have been reported in previous studies.[70,71] On the other hand, CP/CuS@PD-PU shows a uniform temperature distribution, as demonstrated in Figure 6e$_6$, suggesting a uniform distribution of the photothermal material. The uniform distribution of CP/CuS nanoparticles on the foam surface, evident from the SEM image, likely facilitates consistent water transportation, thereby accelerating the vapor evaporation rate. Furthermore, contact angle measurements substantiate this water transportation behavior, which shows the CP/CuS@PD-PU surface to be more hydrophilic than CP@PD-PU and CuS@PD-PU foam surfaces. Even though an elevated temperature is an important factor for evaluating the conversion performance of the photothermal material, it does not solely dictate the evaporation rate. The evaporative surface should have optimal wettability to ensure water replenishment and simultaneously enhance and speed up vapor escape.

Finally, the solar-vapor conversion efficiency (η) was calculated using the following equation.[72,73]

$$\eta = \frac{\dot{m}\Delta H_{vap}}{I}$$

where I is the power density of the incident light (1 kW m^{-2}) and ΔH_{vap} is the evaporation enthalpy of water, calculated as follows

$$\Delta H_{vap} = C\Delta T + h_{LV}$$

where C is the specific heat capacity of water (4.2 kJ °C^{-1} kg^{-1}), ΔT is the temperature increase during vaporization, and h_{LV} is the latent heat of vaporization of water which is taken as 2256 kJ kg^{-1}. It is important to note that to calculate the efficiency, the water evaporation rate in a dark environment (0.164 kg m^{-2} h^{-1}) was subtracted from all measured rates under solar irradiation to remove the effect of natural water evaporation (Figure 6d). CP/CuS@PD-PU demonstrated a solar-to-vapor conversion efficiency of 93.8%, followed by CuS@PD-PU (78.3%), CP@PD-PU (69.1%), and PU-PDA (60.4%). The performance of our evaporator is compared with that of a state-of-the-art steam generation evaporator under 1 sun illumination (Table S1). It was found that our evaporator outperformed most CuS-based evaporators. The high water evaporation rate and solar-vapor conversion efficiency exhibited by our evaporator can be attributed to the following factors: (a) the broad solar absorption and excellent solar-induced heat generation originating from the resonance energy transfer effect showcased by the meticulously designed core–shell CP/CuS heterostructure, (b) the localized heat generation from the confined coating of the photothermal material on the evaporation surface and the reduced heat loss to the bulk due to the well-configured evaporator, and (c) the efficient water replenishment during evaporation facilitated by the balanced hydrophobic-hydrophilic photothermal surface.

CONCLUSIONS

In this study, we designed a core–shell structure, integrating CP with semiconducting copper sulfides (CuS), aiming to enhance the photothermal effect through the FRET mechanism. The proximity between the donor (CP) and acceptor (CuS) within this core–shell structure facilitates this resonance energy transfer, boosting the generation of photothermal energy. With excellent solar absorption and photothermal conversion capabilities, this structure was particularly advantageous for driving interfacial water evaporation. CP/CuS-coated PU foam (CP/CuS@PD-PU) demonstrated a total solar absorption of 97.1% and was able to elevate the surface temperature by 61.6 °C under dry conditions when exposed to solar illumination at a power density of 1 kW m^{-2} (equivalent to 1 sun). The optimal wettability of the CP/CuS@PD-PU surface facilitated consistent water replenishment in the evaporative region, simultaneously accelerating vapor escape. This balanced hydrophobic-hydrophilic nature of the photothermal layer played a vital role in the solar-induced interfacial steam generation process. As a result, under 1 sun illumination, CP/CuS@PD-PU foam exhibited an evaporation rate of 1.62 kg m^{-2} h^{-1} and an energy conversion efficiency of 93.8%. This study focused on enhancing photothermal heat generation via resonance energy transfer in a core–shell structure and offers novel insights into designing unique structures that exhibit superior photothermal properties. These findings could have significant implications for various solar-driven applications.

ASSOCIATED CONTENT

Supporting Information

The Supporting Information is available free of charge at https://pubs.acs.org/doi/10.1021/acsami.3c10778.

FT-IR spectra of CuS, CP, and CP/CuS core–shell heterostructure; SEM micrograph of CuS and CP/CuS heterostructure, TEM image of CP/CuS core–shell heterostructure; dispersion stability of CP, CuS, and CP/CuS core–shell heterostructure in ethanol solution; digital and SEM image of PU foam; high-resolution XPS spectra for PU foam, PD-PU, CuS@PD-PU, CP@PD-PU, and CP/CuS@PD-PU; UV–vis–NIR transmittance and reflectance of pure and coated PU foams; IR thermal images of pure and coated foams under 1 sun solar irradiation; evaporation rate of water under dark environment; summary of the studied samples and their observed properties; and performance comparison of

https://doi.org/10.1021/acsami.3c10778
ACS Appl. Mater. Interfaces 2023, 15, 54773–54785

various steam generation evaporators under solar irradiance with the present work (PDF)

Video demonstrating the dynamics of water spreading and its movement on the CP/CuS@PD-PU foam (MOV)

AUTHOR INFORMATION

Corresponding Author

Woochul Lee − *Department of Mechanical Engineering, University of Hawaii at Manoa, Honolulu, Hawaii 96822, United States;* orcid.org/0000-0002-0911-961X; Email: woochull@hawaii.edu

Authors

Suman Chhetri − *Department of Mechanical Engineering, University of Hawaii at Manoa, Honolulu, Hawaii 96822, United States;* orcid.org/0000-0002-3637-2813

Anh Tuan Nguyen − *Department of Mechanical Engineering, University of Hawaii at Manoa, Honolulu, Hawaii 96822, United States;* orcid.org/0000-0002-1441-9705

Sehwan Song − *Bioinspired Engineering Laboratory, Department of Mechanical Engineering, Inha University, Incheon 22212, Republic of Korea;* orcid.org/0000-0001-6710-577X

Dong Hyuk Park − *Department of Chemical Engineering, Program in Biomedical Science & Engineering, Inha University, Incheon 22212, Republic of Korea*

Tianwei Ma − *College of Engineering, Texas A&M University-Corpus Christi, Corpus Christi, Texas 78412, United States*

Nicolas Gaillard − *Hawaii Natural Energy Institute, University of Hawaii at Manoa, Honolulu, Hawaii 96822, United States;* orcid.org/0000-0002-9665-2948

Sang-Hee Yoon − *Bioinspired Engineering Laboratory, Department of Mechanical Engineering, Inha University, Incheon 22212, Republic of Korea;* orcid.org/0000-0002-6897-7657

Complete contact information is available at: https://pubs.acs.org/10.1021/acsami.3c10778

Author Contributions

S.C.: methodology, data curation, investigation, formal analysis, validation, visualization, writing (original draft). A.T.N.: data curation, formal analysis, writing (review and editing). S.S.: methodology, formal analysis. D.H.P.: formal analysis, writing (review and editing). N.G.: data curation, formal analysis, writing (review and editing). T.M.: funding acquisition, writing (review and editing). S.-H.Y.: data curation, formal analysis, validation, writing (review and editing). W.L.: conceptualization, supervision, writing (review and editing), project administration, funding acquisition.

Notes

The authors declare no competing financial interest.

ACKNOWLEDGMENTS

This research was partially supported by the Hawaii Department of Transportation under project number 2020-2-TCS. W.L. acknowledges support from the National Science Foundation (EEC-2034824). W.L. is grateful for the support from the College of Engineering at the University of Hawaii at Manoa.

REFERENCES

(1) Ren, H.; Tang, M.; Guan, B.; Wang, K.; Yang, J.; Wang, F.; Wang, M.; Shan, J.; Chen, Z.; Wei, D.; Peng, H.; Liu, Z. Hierarchical Graphene Foam for Efficient Omnidirectional Solar-Thermal Energy Conversion. *Adv. Mater.* **2017**, *29* (38), 1702590.

(2) Tao, P.; Ni, G.; Song, C.; Shang, W.; Wu, J.; Zhu, J.; Chen, G.; Deng, T. Solar-Driven Interfacial Evaporation. *Nat. Energy* **2018**, *3* (12), 1031−1041.

(3) Zhou, X.; Guo, Y.; Zhao, F.; Yu, G. Hydrogels as an Emerging Material Platform for Solar Water Purification. *Acc. Chem. Res.* **2019**, *52* (11), 3244−3253.

(4) Zhou, X.; Zhao, F.; Guo, Y.; Rosenberger, B.; Yu, G. Architecting Highly Hydratable Polymer Networks to Tune the Water State for Solar Water Purification. *Sci. Adv.* **2019**, *5* (6), No. eaaw5484.

(5) Ghasemi, H.; Ni, G.; Marconnet, A. M.; Loomis, J.; Yerci, S.; Miljkovic, N.; Chen, G. Solar Steam Generation by Heat Localization. *Nat. Commun.* **2014**, *5* (1), 4449.

(6) Zhang, Y.; Xiong, T.; Nandakumar, D. K.; Tan, S. C. Structure Architecting for Salt-Rejecting Solar Interfacial Desalination to Achieve High-Performance Evaporation With In Situ Energy Generation. *Advanced Science* **2020**, *7* (9), 1903478.

(7) Gao, M.; Zhu, L.; Peh, C. K.; Ho, G. W. Solar Absorber Material and System Designs for Photothermal Water Vaporization towards Clean Water and Energy Production. *Energy Environ. Sci.* **2019**, *12* (3), 841−864.

(8) Tan, M.; Wang, J.; Song, W.; Fang, J.; Zhang, X. Self-Floating Hybrid Hydrogels Assembled with Conducting Polymer Hollow Spheres and Silica Aerogel Microparticles for Solar Steam Generation. *J. Mater. Chem. A* **2019**, *7* (3), 1244−1251.

(9) Lin, Z.; Wu, T.; Feng, Y.-F.; Shi, J.; Zhou, B.; Zhu, C.; Wang, Y.; Liang, R.; Mizuno, M. Poly(N-Phenylglycine)/MoS2 Nanohybrid with Synergistic Solar-Thermal Conversion for Efficient Water Purification and Thermoelectric Power Generation. *ACS Appl. Mater. Interfaces* **2022**, *14* (1), 1034−1044.

(10) Li, B.; Guo, Z.; Feng, Y.; Meng, M. A Multi-Functional Photothermal-Catalytic Foam for Cascade Treatment of Saline Wastewater. *J. Mater. Chem. A* **2021**, *9* (30), 16510−16521.

(11) Shao, B.; Wang, Y.; Wu, X.; Lu, Y.; Yang, X.; Chen, G. Y.; Owens, G.; Xu, H. Stackable Nickel-Cobalt@polydopamine Nanosheet Based Photothermal Sponges for Highly Efficient Solar Steam Generation. *J. Mater. Chem. A* **2020**, *8* (23), 11665−11673.

(12) Zhang, Z.; Mu, P.; He, J.; Zhu, Z.; Sun, H.; Wei, H.; Liang, W.; Li, A. Facile and Scalable Fabrication of Surface-Modified Sponge for Efficient Solar Steam Generation. *ChemSusChem* **2019**, *12* (2), 426−433.

(13) Wang, H.; Lu, Z.; Ma, S.; Li, Z.; Xin, Z.; Zhang, Z.; Zhou, B.; Shen, J.; Qin, L.; Du, A. Ultrablack Poly(Vinyl Alcohol)-Graphite Composite Xerogel with Vertically Arranged Pores for Highly Efficient Solar Steam Generation and Desalination. *Adv. Energy Sustainability Res.* **2022**, *3* (4), 2100188.

(14) Chhetri, S.; Nguyen, A. T.; Song, S.; Gaillard, N.; Severa, G.; Ma, T.; Yoon, S.-H.; Lee, W. Flexible Graphite Nanoflake/Polydimethylsiloxane Nanocomposites with Promising Solar-Thermal Conversion Performance. *ACS Appl. Energy Mater.* **2023**, *6* (4), 2582−2593.

(15) Zhang, P.; Li, J.; Lv, L.; Zhao, Y.; Qu, L. Vertically Aligned Graphene Sheets Membrane for Highly Efficient Solar Thermal Generation of Clean Water. *ACS Nano* **2017**, *11* (5), 5087−5093.

(16) Chen, C.; Li, Y.; Song, J.; Yang, Z.; Kuang, Y.; Hitz, E.; Jia, C.; Gong, A.; Jiang, F.; Zhu, J. Y.; Yang, B.; Xie, J.; Hu, L. Highly Flexible and Efficient Solar Steam Generation Device. *Adv. Mater.* **2017**, *29* (30), 1701756.

(17) Hu, X.; Xu, W.; Zhou, L.; Tan, Y.; Wang, Y.; Zhu, S.; Zhu, J. Tailoring Graphene Oxide-Based Aerogels for Efficient Solar Steam Generation under One Sun. *Adv. Mater.* **2017**, *29* (5), 1604031.

(18) Linic, S.; Aslam, U.; Boerigter, C.; Morabito, M. Photochemical Transformations on Plasmonic Metal Nanoparticles. *Nat. Mater.* **2015**, *14* (6), 567−576.

(19) Liang, J.; Liu, H.; Yu, J.; Zhou, L.; Zhu, J. Plasmon-Enhanced Solar Vapor Generation. *Nanophotonics* **2019**, *8* (5), 771−786.
(20) Zhang, F.; Li, Y.-H.; Qi, M.-Y.; Yamada, Y. M. A.; Anpo, M.; Tang, Z.-R.; Xu, Y.-J. Photothermal Catalytic CO2 Reduction over Nanomaterials. *Chem Catal.* **2021**, *1* (2), 272−297.
(21) Zhu, G.; Xu, J.; Zhao, W.; Huang, F. Constructing Black Titania with Unique Nanocage Structure for Solar Desalination. *ACS Appl. Mater. Interfaces* **2016**, *8* (46), 31716−31721.
(22) Huang, W.; Su, P.; Cao, Y.; Li, C.; Chen, D.; Tian, X.; Su, Y.; Qiao, B.; Tu, J.; Wang, X. Three-Dimensional Hierarchical CuxS-Based Evaporator for High-Efficiency Multifunctional Solar Distillation. *Nano Energy* **2020**, *69*, 104465.
(23) An, L.; Wang, C.; Feng, Q.; Xu, Z.; Tian, Q.; Chai, W.; Yang, S.; Bian, Z. A Flexible Copper Sulfide Composite Membrane with Tunable Plasmonic Resonance Absorption for Near-Infrared Light-Driven Seawater Desalination. *Environ. Sci.: Adv.* **2022**, *1* (2), 110−120.
(24) Tao, F.; Zhang, Y.; Yin, K.; Cao, S.; Chang, X.; Lei, Y.; Wang, D. S.; Fan, R.; Dong, L.; Yin, Y.; Chen, X. Copper Sulfide-Based Plasmonic Photothermal Membrane for High-Efficiency Solar Vapor Generation. *ACS Appl. Mater. Interfaces* **2018**, *10* (41), 35154−35163.
(25) Zhao, Q.; Wan, Y.; Chang, F.; Wang, Y.; Jiang, H.; Jiang, L.; Zhang, X.; Ma, N. Photothermal Converting Polypyrrole/Polyurethane Composite Foams for Effective Solar Desalination. *Desalination* **2022**, *527*, 115581.
(26) Wang, X.; Liu, Q.; Wu, S.; Xu, B.; Xu, H. Multilayer Polypyrrole Nanosheets with Self-Organized Surface Structures for Flexible and Efficient Solar-Thermal Energy Conversion. *Adv. Mater.* **2019**, *31* (19), 1807716.
(27) Guo, L.; Gong, J.; Song, C.; Zhao, Y.; Tan, B.; Zhao, Q.; Jin, S. Donor-Acceptor Charge Migration System of Superhydrophilic Covalent Triazine Framework and Carbon Nanotube toward High Performance Solar Thermal Conversion. *ACS Energy Lett.* **2020**, *5* (4), 1300−1306.
(28) Irshad, M. S.; Wang, X.; Abbas, A.; Yu, F.; Li, J.; Wang, J.; Mei, T.; Qian, J.; Wu, S.; Javed, M. Q. Salt-Resistant Carbon Dots Modified Solar Steam System Enhanced by Chemical Advection. *Carbon* **2021**, *176*, 313−326.
(29) Guo, J.; Liang, Y.; Liu, L.; Hu, J.; Wang, H.; An, W.; Cui, W. Core-Shell Structure of Sulphur Vacancies-CdS@CuS: Enhanced Photocatalytic Hydrogen Generation Activity Based on Photoinduced Interfacial Charge Transfer. *J. Colloid Interface Sci.* **2021**, *600*, 138−149.
(30) Zhang, L.-X.; Qi, M.-Y.; Tang, Z.-R.; Xu, Y.-J. Heterostructure-Engineered Semiconductor Quantum Dots toward Photocatalyzed-Redox Cooperative Coupling Reaction. *Research* **2023**, *6*, 0073.
(31) Li, Y.-H.; Qi, M.-Y.; Li, J.-Y.; Tang, Z.-R.; Xu, Y.-J. Noble Metal Free CdS@CuS-NixP Hybrid with Modulated Charge Transfer for Enhanced Photocatalytic Performance. *Appl. Catal., B* **2019**, *257*, 117934.
(32) Li, S.-H.; Qi, M.-Y.; Tang, Z.-R.; Xu, Y.-J. Nanostructured Metal Phosphides: From Controllable Synthesis to Sustainable Catalysis. *Chem. Soc. Rev.* **2021**, *50* (13), 7539−7586.
(33) Chen, W.; Liang, X.; Fu, W.; Wang, S.; Gao, X.; Zhang, Z.; Fang, Y. Phase Change Composite with Core-Shell Structure for Photothermal Conversion and Thermal Energy Storage. *ACS Appl. Energy Mater.* **2022**, *5* (7), 9109−9117.
(34) Ma, K.; Li, Y.; Wang, Z.; Chen, Y.; Zhang, X.; Chen, C.; Yu, H.; Huang, J.; Yang, Z.; Wang, X.; Wang, Z. Core-Shell Gold Nanorod@Layered Double Hydroxide Nanomaterial with Highly Efficient Photothermal Conversion and Its Application in Antibacterial and Tumor Therapy. *ACS Appl. Mater. Interfaces* **2019**, *11* (33), 29630−29640.
(35) Zheng, Z.; Li, W.; Liu, H.; Wang, X. Sustainable Interfacial Evaporation System Based on Hierarchical MXene/Polydopamine/Magnetic Phase-Change Microcapsule Composites for Solar-Driven Seawater Desalination. *ACS Appl. Mater. Interfaces* **2022**, *14* (45), 50966−50981.
(36) Chen, S.; Zheng, Z.; Liu, H.; Wang, X. Highly Efficient, Antibacterial, and Salt-Resistant Strategy Based on Carbon Black/Chitosan-Decorated Phase-Change Microcapsules for Solar-Powered Seawater Desalination. *ACS Appl. Mater. Interfaces* **2023**, *15* (13), 16640−16653.
(37) Shen, H.; Zheng, Z.; Liu, H.; Wang, X. A Solar-Powered Interfacial Evaporation System Based on MoS_2 -Decorated Magnetic Phase-Change Microcapsules for Sustainable Seawater Desalination. *J. Mater. Chem. A* **2022**, *10* (48), 25509−25526.
(38) Liu, H.; Tian, D.; Zheng, Z.; Wang, X.; Qian, Z. MXene-Decorated Magnetic Phase-Change Microcapsules for Solar-Driven Continuous Seawater Desalination with Easy Salt Accumulation Elimination. *Chem. Eng. J.* **2023**, *458*, 141395.
(39) Tan, M.; Li, X.; Zhang, H.; Zheng, M.; Xiong, J.; Cao, Y.; Cao, G.; Wang, Z.; Ran, H. Förster Resonance Energy Transfer Nanobullet for Photoacoustic Imaging and Amplified Photothermal-Photodynamic Therapy of Cancer. *Adv. Healthcare Mater.* **2023**, *12*, 2202943.
(40) Wang, Y.; Shang, B.; Hu, X.; Peng, B.; Deng, Z. Temperature Control of Mussel-Inspired Chemistry toward Hierarchical Superhydrophobic Surfaces for Oil/Water Separation. *Adv. Mater. Interfaces* **2017**, *4* (2), 1600727.
(41) Chhetri, S.; Sarwar, A.; Steer, J.; Dhib, R.; Bougherara, H. Design of a Bi-Layer Coating Configuration on Ultra-High Molecular Weight Adv. Healthcare Mater.Polyethylene (UHMWPE) Fibre Surface to Derive Synergistic Response on Interfacial Bond Strength. *Composites, Part A* **2022**, *152*, 106678.
(42) Zhou, H.; Xue, C.; Chang, Q.; Yang, J.; Hu, S. Assembling Carbon Dots on Vertically Aligned Acetate Fibers as Ideal Salt-Rejecting Evaporators for Solar Water Purification. *Chem. Eng. J.* **2021**, *421*, 129822.
(43) Pei, L. Z.; Wang, J. F.; Tao, X. X.; Wang, S. B.; Dong, Y. P.; Fan, C. G.; Zhang, Q.-F. Synthesis of CuS and Cu1.1Fe1.1S2 Crystals and Their Electrochemical Properties. *Mater. Charact.* **2011**, *62* (3), 354−359.
(44) De, B.; Balamurugan, J.; Kim, N. H.; Lee, J. H. Enhanced Electrochemical and Photocatalytic Performance of Core-Shell CuS@Carbon Quantum Dots@Carbon Hollow Nanospheres. *ACS Appl. Mater. Interfaces* **2017**, *9* (3), 2459−2468.
(45) Pol, V. G.; Thackeray, M. M. Spherical Carbon Particles and Carbon Nanotubes Prepared by Autogenic Reactions: Evaluation as Anodes in Lithium Electrochemical Cells. *Energy Environ. Sci.* **2011**, *4* (5), 1904−1912.
(46) Sergiienko, R.; Shibata, E.; Kim, S.; Kinota, T.; Nakamura, T. Nanographite Structures Formed during Annealing of Disordered Carbon Containing Finely-Dispersed Carbon Nanocapsules with Iron Carbide Cores. *Carbon* **2009**, *47* (4), 1056−1065.
(47) Chen, J.; Yin, J. L.; Li, B.; Ye, Z.; Liu, D.; Ding, D.; Qian, F.; Myung, N. V.; Zhang, Q.; Yin, Y. Janus Evaporators with Self-Recovering Hydrophobicity for Salt-Rejecting Interfacial Solar Desalination. *ACS Nano* **2020**, *14* (12), 17419−17427.
(48) Zhang, Y.; Yin, X.; Yu, B.; Wang, X.; Guo, Q.; Yang, J. Recyclable Polydopamine-Functionalized Sponge for High-Efficiency Clean Water Generation with Dual-Purpose Solar Evaporation and Contaminant Adsorption. *ACS Appl. Mater. Interfaces* **2019**, *11* (35), 32559−32568.
(49) Han, D.-L.; Yu, P.-L.; Liu, X.-M.; Xu, Y.-D.; Wu, S.-L. Polydopamine Modified CuS@HKUST for Rapid Sterilization through Enhanced Photothermal Property and Photocatalytic Ability. *Rare Met.* **2022**, *41* (2), 663−672.
(50) Zhu, R.; Liu, M.; Hou, Y.; Wang, D.; Zhang, L.; Wang, D.; Fu, S. Mussel-Inspired Photothermal Synergetic System for Clean Water Production Using Full-Spectrum Solar Energy. *Chem. Eng. J.* **2021**, *423*, 129099.
(51) Yu, T.; Halouane, F.; Mathias, D.; Barras, A.; Wang, Z.; Lv, A.; Lu, S.; Xu, W.; Meziane, D.; Tiercelin, N.; Szunerits, S.; Boukherroub, R. Preparation of Magnetic, Superhydrophobic/Superoleophilic Polyurethane Sponge: Separation of Oil/Water Mixture and Demulsification. *Chem. Eng. J.* **2020**, *384*, 123339.

https://doi.org/10.1021/acsami.3c10778
ACS Appl. Mater. Interfaces 2023, 15, 54773−54785

(52) Li, Y.; Zhao, R.; Chao, S.; Sun, B.; Wang, C.; Li, X. Polydopamine Coating Assisted Synthesis of MnO2 Loaded Inorganic/Organic Composite Electrospun Fiber Adsorbent for Efficient Removal of Pb2+ from Water. *Chem. Eng. J.* **2018**, *344*, 277−289.
(53) Chen, J.; Wang, Q.; Luan, M.; Mo, J.; Yan, Y.; Li, X. Polydopamine as Reinforcement in the Coating of Nano-Silver on Polyurethane Surface: Performance and Mechanisms. *Prog. Org. Coat.* **2019**, *137*, 105288.
(54) Ludwig, J.; An, L.; Pattengale, B.; Kong, Q.; Zhang, X.; Xi, P.; Huang, J. Ultrafast Hole Trapping and Relaxation Dynamics in P-Type CuS Nanodisks. *J. Phys. Chem. Lett.* **2015**, *6* (14), 2671−2675.
(55) Chang, Q.; Guo, Z.; Shen, Z.; Li, N.; Xue, C.; Zhang, H.; Hao, C.; Yang, J.; Hu, S. Interaction Promotes the Formation and Photothermal Conversion of Carbon Dots/Polydopamine Composite for Solar-Driven Water Evaporation. *Adv. Mater. Interfaces* **2021**, *8* (12), 2100332.
(56) Tian, Q.; Tang, M.; Sun, Y.; Zou, R.; Chen, Z.; Zhu, M.; Yang, S.; Wang, J.; Wang, J.; Hu, J. Hydrophilic Flower-Like CuS Superstructures as an Efficient 980 Nm Laser-Driven Photothermal Agent for Ablation of Cancer Cells. *Adv. Mater.* **2011**, *23* (31), 3542−3547.
(57) Gao, J.; Li, Q.; Zhao, H.; Li, L.; Liu, C.; Gong, Q.; Qi, L. One-Pot Synthesis of Uniform Cu $_2$ O and CuS Hollow Spheres and Their Optical Limiting Properties. *Chem. Mater.* **2008**, *20* (19), 6263−6269.
(58) Sun, M.; Kreis, N.; Chen, K.; Fu, X.; Guo, S.; Wang, H. Covellite Nanodisks and Digenite Nanorings: Colloidal Synthesis, Phase Transitions, and Optical Properties. *Chem. Mater.* **2021**, *33* (21), 8546−8558.
(59) Shang, M.; Li, N.; Zhang, S.; Zhao, T.; Zhang, C.; Liu, C.; Li, H.; Wang, Z. Full-Spectrum Solar-to-Heat Conversion Membrane with Interfacial Plasmonic Heating Ability for High-Efficiency Desalination of Seawater. *ACS Appl. Energy Mater.* **2018**, *1* (1), 56−61.
(60) Wu, X.; Robson, M. E.; Phelps, J. L.; Tan, J. S.; Shao, B.; Owens, G.; Xu, H. A Flexible Photothermal Cotton-CuS Nanocage-Agarose Aerogel towards Portable Solar Steam Generation. *Nano Energy* **2019**, *56*, 708−715.
(61) Luther, J. M.; Jain, P. K.; Ewers, T.; Alivisatos, A. P. Localized Surface Plasmon Resonances Arising from Free Carriers in Doped Quantum Dots. *Nat. Mater.* **2011**, *10* (5), 361−366.
(62) Sun, M.; Fu, X.; Chen, K.; Wang, H. Dual-Plasmonic Gold@Copper Sulfide Core-Shell Nanoparticles: Phase-Selective Synthesis and Multimodal Photothermal and Photocatalytic Behaviors. *ACS Appl. Mater. Interfaces* **2020**, *12* (41), 46146−46161.
(63) Chang, Q.; Shen, Z.; Guo, Z.; Xue, C.; Li, N.; Yang, J.; Hu, S. Hydroxypropylmethyl Cellulose Modified with Carbon Dots Exhibits Light-Responsive and Reversible Optical Switching. *ACS Appl. Mater. Interfaces* **2021**, *13* (10), 12375−12382.
(64) Liang, Z.; Kang, M.; Payne, G. F.; Wang, X.; Sun, R. Probing Energy and Electron Transfer Mechanisms in Fluorescence Quenching of Biomass Carbon Quantum Dots. *ACS Appl. Mater. Interfaces* **2016**, *8* (27), 17478−17488.
(65) Surana, K.; Bhattacharya, B. Fluorescence Quenching by Förster Resonance Energy Transfer in Carbon-Cadmium Sulfide Core-Shell Quantum Dots. *ACS Omega* **2021**, *6* (48), 32749−32753.
(66) Ji, M.; Liu, H.; Cheng, M.; Huang, L.; Yang, G.; Bao, F.; Huang, G.; Huang, Y.; Hu, Y.; Cong, G.; Yu, J.; Zhu, C.; Xu, J. Plasmonic Metal Nanoparticle Loading to Enhance the Photothermal Conversion of Carbon Fibers. *J. Phys. Chem. C* **2022**, *126* (5), 2454−2462.
(67) Xu, M.; Tu, G.; Ji, M.; Wan, X.; Liu, J.; Liu, J.; Rong, H.; Yang, Y.; Wang, C.; Zhang, J. Vacuum-Tuned-Atmosphere Induced Assembly of Au@Ag Core/Shell Nanocubes into Multi-Dimensional Superstructures and the Ultrasensitive IAPP Proteins SERS Detection. *Nano Res.* **2019**, *12* (6), 1375−1379.
(68) Zhang, L.; Xu, X.; Feng, J.; Bai, B.; Hu, N.; Wang, H. Waste semi-coke/polydopamine based self-floating solar evaporator for water purification. *Sol. Energy Mater. Sol.* **2021**, *230*, 111237.
(69) Su, L.; Hu, Y.; Ma, Z.; Miao, L.; Zhou, J.; Ning, Y.; Chang, Z.; Wu, B.; Cao, M.; Xia, R.; Qian, J. Synthesis of hollow copper sulfide nanocubes with low emissivity for highly efficient solar steam generation. *Sol. Energy Mater. Sol.* **2020**, *210*, 110484.
(70) Meng, S.; Zha, X.-J.; Wu, C.; Zhao, X.; Yang, M.-B.; Yang, W. Interfacial Radiation-Absorbing Hydrogel Film for Efficient Thermal Utilization on Solar Evaporator Surfaces. *Nano Lett.* **2021**, *21* (24), 10516−10524.
(71) Xue, C.; Li, P.; Zhang, Q.; Li, D.; Li, Y.; Chang, Q.; Yang, J.; Li, Y.; Zhang, J.; Hu, S. Fabrication of High-Performance Graphene Oxide/CuO/Cu2O Film-Coated Copper Foam for Interfacial Solar-Driven Water Evaporation. *J. Mater. Sci.* **2022**, *57* (5), 3322−3336.
(72) Chen, J.; Li, B.; Hu, G.; Aleisa, R.; Lei, S.; Yang, F.; Liu, D.; Lyu, F.; Wang, M.; Ge, X.; Qian, F.; Zhang, Q.; Yin, Y. Integrated Evaporator for Efficient Solar-Driven Interfacial Steam Generation. *Nano Lett.* **2020**, *20* (8), 6051−6058.
(73) Fan, Y.; Tian, Z.; Wang, F.; He, J.; Ye, X.; Zhu, Z.; Sun, H.; Liang, W.; Li, A. Enhanced Solar-to-Heat Efficiency of Photothermal Materials Containing an Additional Light-Reflection Layer for Solar-Driven Interfacial Water Evaporation. *ACS Appl. Energy Mater.* **2021**, *4* (3), 2932−2943.

https://doi.org/10.1021/acsami.3c10778
ACS Appl. Mater. Interfaces 2023, 15, 54773−54785